Materials Today Chemistry 29 (2023) 101455

Contents lists available at ScienceDirect

Materials Today Chemistry

journal homepage: www.journals.elsevier.com/materials-today-chemistry/

PEA_2PbI_4: fast two-dimensional lead iodide perovskite scintillator with green and red emission

D. Kowal [a], M. Makowski [b], M.E. Witkowski [b], R. Cala' [c, d], M.A. Kuddus Sheikh [a], M.H. Mahyuddin [e], E. Auffray [c], W. Drozdowski [b], D. Cortecchia [f, g, *], M.D. Birowosuto [a, **]

[a] Łukasiewicz Research Network-PORT Polish Center for Technology Development, Stabłowicka 147, Wrocław, 54-066, Poland
[b] Institute of Physics, Faculty of Physics, Astronomy, and Informatics, Nicolaus Copernicus University in Torun, Ul. Grudziadzka 5, Torun, 87-100, Poland
[c] CERN, Esplanade des Particules 1, Meyrin, 1211, Switzerland
[d] Università Degli Studi di Milano-Bicocca, Piazza Della Scienza 3, Milano, 20126, Italy
[e] Faculty of Mathematics and Natural Sciences, Institut Teknologi Bandung, Jl. Ganesha 10, Bandung, 40132, Indonesia
[f] Istituto Italiano di Tecnologia, Center for Nano Science and Technology (CNST@PoliMi), Via Pascoli 70, Milan, 20133, Italy
[g] Dipartimento di Chimica Industriale Toso Montanari, Universita di Bologna, 40136 Bologna, Italy

ARTICLE INFO

Article history:
Received 26 October 2022
Received in revised form
23 January 2023
Accepted 13 February 2023
Available online 13 March 2023

Keywords:
2D perovskites
Scintillators
Scintillation lifetime
X-ray imaging
Time-of-flight positron emission tomography

ABSTRACT

Among the two-dimensional hybrid organic-inorganic perovskites, PEA_2PbBr_4 is one of the best scintillators combining high light yield and fast nanosecond decay time. However, it has limited sensitivity to X-ray and positron emission tomography because of insufficient mass density and effective atomic number. In this article, we show that exchanging the halide from bromide to iodide allows to shorten the absorption length as much as two times for X-ray energies. We present a detailed study on scintillation properties of self-grown samples of PEA_2PbI_4 crystal, which we compare with the previously reported results for PEA_2PbBr_4 crystal. The synthesis method of PEA_2PbI_4 crystal is based on dissolving the perovskite precursors in hydroiodic acid, which is then stirred and left for evaporation. Our measurements include the characterizations with optical, X-ray, and γ-ray sources. We observe two emission bands of PEA_2PbI_4 crystal centered at 532 (green) and 660 (red) nm, and we link them to the scintillation mechanisms involving exciton and surface defect states. We also report the scintillation light yields of 1,000 and 10,000 photons/MeV at room temperature and 10 K, respectively, and the coincidence timing resolution full width at half maximum of 138 ps, and the fast component in scintillation decay curve of 0.5 ns. This fast component is much faster than that of 13.4 ns of PEA_2PbBr_4 crystal, and with two times shorter absorption length, it secures better opportunities in timing applications in particular time-of-flight positron emission tomography and high energy physics.

1. Introduction

Two-dimensional (2D) hybrid organic-inorganic perovskite (HOIP) crystals have great interests as scintillating materials [1,2]. They offer multiple advantages for X- and γ-ray scintillation, specifically much shorter absorption length (ℓ) in comparison with that in plastic scintillators because of the presence of lead (Pb) increasing mass density (ρ) and effective atomic number (Z_{eff}), small optical bandgaps between 2 and 4 eV providing platforms for high light yield scintillators, large exciton binding energy around few hundred times than that of three-dimensional (3D) HOIP resulting less prone to thermal quenching for maintaining high light yield at room temperature (RT), the extremely fast scintillation decay time in the order of nanoseconds for spectral and timing applications, and finally, the unusually large Stokes shift of 2D HOIP crystals preventing self-absorption of luminescence [3,4].

Among some investigated 2D HOIP crystals [5], PEA_2PbBr_4 crystals have promising scintillation properties, such as high light yields above 10,000 photons/MeV, energy resolutions below 10% at 662 keV, and fast scintillation decay times below 15 ns [2]. Doping the crystals with lithium (Li), light yield becomes double, whereas the best energy resolution for solution-processable 2D HOIP scintillators becomes 7.7% at 662 keV [6,7]. Such Li-doped PEA_2PbBr_4

* Corresponding author.
** Corresponding author.
E-mail addresses: daniele.cortecchia2@unibo.it (D. Cortecchia), muhammad.birowosuto@port.lukasiewicz.gov.pl (M.D. Birowosuto).

https://doi.org/10.1016/j.mtchem.2023.101455

crystals also exhibit sub-100-ps coincidence timing resolution (CTR) because of their high light yield and nanosecond decay time, and thus, it can be useful for time-of-flight positron emission tomography (TOF PET) [8].

With the ρ and Z_{eff} of 2.36 g/cm^3 and 32.31, respectively, ℓ values of PEA_2PbBr_4 crystals still need to be improved for the sensitivity of X-ray imaging and TOF PET [9], even for the heterostructure configuration [10]. To improve ℓ, we need to use short organic ligand or mix it with inorganic cation [11,12]. However, larger improvement is expected with replacing bromide with iodide, as this anion has always been the final interest in searching halide scintillators if one considers radiation absorption [13–15]. The smaller bandgap in iodides in comparison to that in bromides also may give higher light yield. However, the high light yield in iodides is not always the case as additional quenching mechanism may occur [16]. Finally, the shift of the emission to longer wavelength than that of bromides will increase the detection efficiency of the common detectors in both X-ray imaging and TOF PET applications. For the above reasons introducing iodine anion to one of the best up-to-date 2D HOIP scintillators of PEA_2PbBr_4 and examining its scintillation properties in detail might be the next important step in the development of 2D perovskite scintillators. For 2D HOIP, besides the recent short compilation works of iodide crystals [5], there is hitherto no complete study on the scintillation properties of the PEA_2PbI_4.

Here, we present comprehensive material characteristics of PEA_2PbI_4 crystal, starting with the crystal structure derived from X-ray diffraction experiments and calculation of absorption length (ℓ). We show the expected decrease of ℓ associated with the halide exchange from Br to I. We then demonstrate optical characterization, including photoluminescence (PL) spectra, time-resolved PL (TRPL) decay measurements and absorption. We observe the PL spectrum as a combination of green narrowband and red broadband emission bands, a behavior that has been repeatedly observed for the 2D HOIP in the past [17–19]. From the data analysis, we get the experimental number of bandgap energy E_g^{exp}, which is in good agreement with the theoretical number E_g^{cal} that was obtained from our density functional theory (DFT) calculations. Finally, we show the X-ray and γ-ray scintillation properties of PEA_2PbI_4 crystal, such as radioluminescence (RL) map for different temperatures, thermoluminescence (TL), pulse height, scintillation decay curve, and CTR. Based on our measurements, we report the scintillation light yields, decay components and energy resolution that we compare with previously reported data for PEA_2PbBr_4. Although the observed light yield and energy resolution do not surpass the excellent properties of PEA_2PbBr_4, the PEA_2PbI_4 shows bigger potential for fast-timing applications with much faster scintillation decay components. Thus, we make comparison of scintillation properties of PEA_2PbI_4 and barium fluoride (BaF_2), a commercial scintillator used for fast-timing scintillation applications, for example, TOF PET and high energy physics where PEA_2PbI_4 could become a low-cost alternative in the future.

2. Experimental section

2.1. Synthesis of PEA_2PbI_4 and PEA_2PbBr_4

Hydroiodic acid (HI, 57% w/w aqueous solution, stabilized, Alfa Aesar), phenethylamine (PEA, 99%, Sigma Aldrich), lead oxide (PbO, 99.999%, Sigma Aldrich), and hypophosphorous acid (H_3PO_2, 50% wt in water, Sigma Aldrich) were used for the synthesis. The precursor solution was prepared by dissolving equal molar amounts of PEA (1 mmol) and PbO (1 mmol) in HI (5.5 mL) with the addition of 0.17 mL of H_3PO_2. The solution was stirred at 100°C for 30 min, then it was transferred to an oven and slowly cooled from 100°C to 25°C in 30 h, obtaining large orange perovskite crystals. The crystals precipitated were then collected by filtration and thoroughly dried under vacuum for 3 h. The perovskite was then stored in glovebox under nitrogen before further characterization. It should be emphasized that above-presented synthesis method allows for growing PEA_2PbI_4 crystals of optimized quality and scintillation performance as the optoelectronic properties of PEA_2PbI_4 have been observed to vary with the synthesis method [18]. The synthesis of control PEA_2PbBr_4 crystal was performed by preparing the 3 M molar concentration solution of PEA (Br) and $PbBr_2$ in dimethyl sulfoxide (DMSO), which was stirred at 100°C for 2 h under N_2 atmosphere. The solution was then left for 2 weeks until the solvent evaporated and crystals formed [7].

2.2. X-ray diffraction

Powder X-ray diffraction (XRD) data were recorded on a Bruker D8 Advance AXS diffractometer with graphite-monochromatized Cu Kα radiation (λ = 1.5418 Å). The data acquisition was undertaken at RT under Bragg-Brentano geometry with the speed of scanning as 1 s per step and a step size of 0.02. XRD diffractograms were then analyzed using FullProf software.

2.3. PL, TRPL, and absorption

PL measurements were performed at RT using free-space excitation and collection through a visible-near-infrared microscope objective (Nikon 20 ×; Nikon Corporation, Tokyo, Japan; NA = 0.40). The sample was excited via a 30 kHz ps pulsed diode laser (Master Oscillator Fibre Amplifier, PicoQuant GmbH, Berlin, Germany, excitation wavelength at 375 or 532 nm, pulse width 50 ps, and power of 10 μW). PL spectra were recorded using a high-sensitivity Ocean Pro spectrometer (Ocean Optics Inc, Florida, USA). For TRPL measurements, picosecond pulsed diode lasers with repetition rates of 10 MHz from both excitation wavelengths of 375 nm were used. The emission was then selected by a band filter at 532 ± 25 nm and detected by a single-photon avalanche photodiode (APD) connected to a time-correlated single-photon counting acquisition module (MPD and HydraHarp 400; PicoQuant GmbH, Berlin, Germany). Absorption spectra of perovskite crystals were obtained using the same spectrometer used for the emission, but we modified the setup with homemade white-light source.

2.4. RL, TL, and glow curves

For all these measurements, we used one integrated setup. It consists of an Inel XRG3500 X-ray generator Cu-anode tube, 45 kV/10 mA, an Acton Research Corporation SpectraPro-500i monochromator, a Hamamatsu R928 photomultiplier tube (PMT), and an APD Cryogenic Inc. closed-cycle helium cooler. First, we recorded low-temperature afterglow at 10 K by exposing the crystals to X-rays for 10 min. Then, we measured TL glow curves at temperatures between 10 and 350 K with a heating rate of about 0.14 K/s. Afterward, we measured the RL at different temperatures between 350 and 10 K starting from the highest to lowest temperatures to avoid possible contributions to the emission yield from the thermal release of charge carriers.

2.5. Pulse height and scintillation decay measurements

We used ^{137}Cs (662 keV) radioisotope for γ-ray source and Hamamatsu R878 PMT for detecting the converted photons. The crystal was put in the PMT window without optical coupling due to the strong hygroscopicity. To operate the PMT, we applied a voltage

of 1.25 kV. The corresponding output signal from PMT is integrated with a charge-sensitive pre-amplifier. The output then feeds a spectroscopic amplifier with a shaping time of 2 μs and an analog-to-digital converter (Ortec series). The photoelectron yield was obtained by comparing the position of photopeak to the position of the mean value of the single electron response in pulse high spectra measurements. The actual light yield for the radiation conversion in photons per MeV was obtained after the photoelectron yield was divided by the quantum efficiencies of the PMT. Scintillation decay measurements were performed by the delayed coincidence single photon counting method [5]. $A^{137}Cs$ radioactive source, two Hamamatsu PMTs (R1104 and R928 for "starts" and "stops", respectively), a Canberra 2145 time-to-amplitude converter, and a TUKAN-8K-USB multichannel analyzer were used.

2.6. CTR measurements

The experimental setup to measure CTR of the samples is described in Ref. [8]. The PEA_2PbI_4 crystal was wrapped in several layers of Teflon and coupled to a 3 × 3 mm^2 HPK S13360-3050 Hamamatsu SiPM (biased at 61 V) without optical coupling due to its hygroscopicity. Cargille Meltmount optical coupling was indeed used in previous PEA_2PbBr_4 CTR measurements because the crystal is not hygroscopic [8]. Therefore, without optical coupling, the light yield is between 15 and 20% less than that with optical coupling [20]. The photodetection efficiency curve of the SiPM was multiplied, with the normalized PL spectrum of PEA_2PbI_4 for obtaining spectral efficiency. PEA_2PbI_4 crystal was measured in coincidence with a 2 × 2 × 3 mm^2 LSO:Ce:0.4%Ca reference scintillator attached to an FBK NUV-HD SiPM using Cargille Meltmount. $A^{22}Na$ source was placed between the reference and the measured sample. The SiPM signal was split in two: one part (energy signal) amplified with an operational amplifier and the other (timing signal) amplified with a custom-made high-frequency amplifier [21,22]. A DDA735Zi LeCroy oscilloscope (3.5 GHz bandwidth and 20 Gs/s sampling rate, i.e. 50 ps binning) was then used to digitize the timing and energy signals. A leading edge threshold was set on the oscilloscope to evaluate the signal crossing time (timing signal) by linear interpolation and therefore calculating the delay times of the events detected in coincidence [8].

2.7. DFT calculations

The Kohn–Sham formulation [23] as implemented in the Vienna Ab initio Simulation Package [24,25] was used for the DFT calculations. The Projector Augmented Wave method [26,27] was used to describe the interaction between ion cores and electrons. The electron exchange–correlation was treated by the generalized gradient approximation based on the Perdew–Burke–Ernzerhof functional [28]. The plane wave basis sets with a cut-off energy of 500 eV were used for all calculations. The Brillouin zone with a k-point grid of 5 × 5 × 1 according to the Monkhorst–Pack scheme [29] was used. DFT-D3 method was adopted to account for the dispersion correction [30]. The conjugate gradient method was used for cell optimizations, and the calculations were considered to converge when the maximum forces on each atom were less than 0.01 $eVÅ^{-1}$. During calculations, all atoms were allowed to be fully relaxed.

3. Results and discussion

Fig. 1a shows the appearance of PEA_2PbI_4 and PEA_2PbBr_4 crystals, PEA_2PbI_4 crystal emission, details of the structures, the absorption length, and DFT calculations. The sample of PEA_2PbI_4 is a single crystal with the approximated size of 10 × 5 × 1 mm^3, which

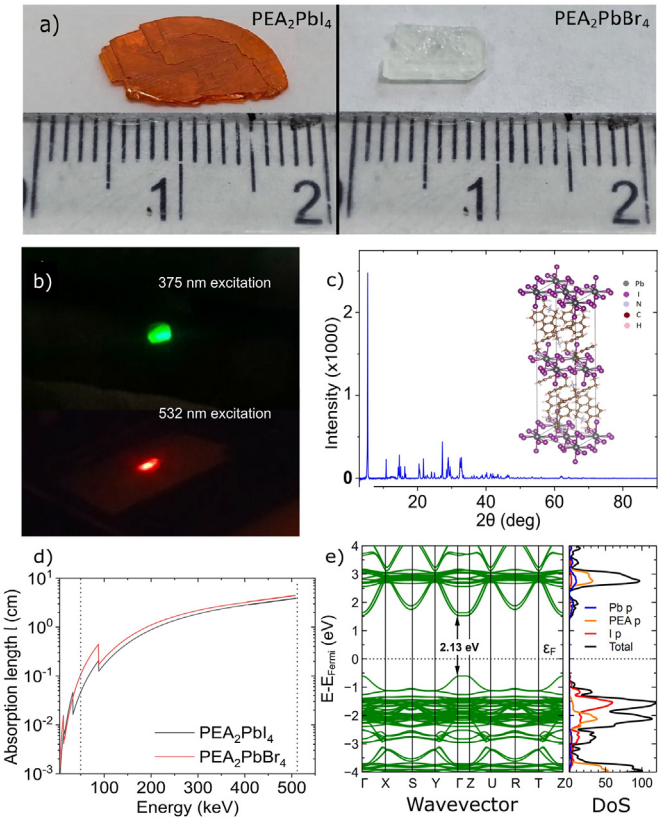

Fig. 1. (a) Photographs of PEA_2PbI_4 and PEA_2PbBr_4 crystals used in the measurements, (b) photograph of PEA_2PbI_4 crystal illuminated with laser at 375 or 532 nm excitation. (c) X-ray diffraction pattern of the single crystal of PEA_2PbI_4 with the inset showing its crystal structure. (d) Calculated absorption lengths as a function of photon energy, covering the X- and γ-ray spectral regions for PEA_2PbI_4 and PEA_2PbBr_4. (e) The band structure, total (black) and projected (color) density of states of PEA_2PbI_4. Blue, orange, and red lines represent Pb p, PEA p and I p, respectively.

can be larger than that of PEA_2PbBr_4. PEA_2PbI_4 crystal exhibits orange color while its emission is green or red when we excited with ultraviolet or green excitation, respectively (Fig. 1b). In general, the emission is shifted to longer wavelength in comparison with blue emission of PEA_2PbBr_4 crystal, which is more than two times better in spectral efficiency for the detection with visible SiPM [8] or photodiode readout [14]. The XRD lines in Fig. 1c were analyzed by Rietveld refinement using FullProf software with the previous model of PEA_2PbI_4 [18,31], and the results are shown in Fig. S1 and Table S1. The triclinic phase can be found with P1 space group and redefined lattice parameters of PEA_2PbI_4 (a = 8.5835 Å, b = 8.6833 Å, c = 33.2053 Å). This phase still belongs to the general class of A_2PbX_4 (X = I, Br, Cl and A = organic cation) HOIP crystals and consists of the stack of ⟨100⟩ oriented perovskite inorganic layers, forming a two-dimensional (2D) Pb-X octahedra network in alternation with the organic sheets of $C_6H_5(CH_2)_2NH_3^+$ cations. The observed mismatches in peak intensities are very small due to considerable texture in the samples obtained from finely ground crystals for the XRD measurements, whereas the reconstructed structure is shown in the inset of Fig. 1c. In our works, the lattice parameters of a and b are shorter between 1% and 2% in comparison to those reported in Ref. [31]. This new calculation yields slightly larger ρ of 2.59 g/cm^3 than that of 2.55 g/cm^3 in Ref. [31] and that of 2.36 g/cm^3 for PEA_2PbBr_4. As a result, ℓ values of PEA_2PbI_4 crystals are much shorter than those of PEA_2PbBr_4 crystals as shown in Fig. 1d. At 50 keV related with X-ray imaging, ℓ of PEA_2PbI_4 is

0.05 cm, two times shorter than ℓ of PEA_2PbBr_4 of 0.11 cm. The halide effect is becoming less for ℓ at 511 keV as they are 3.91 and 4.47 cm for PEA_2PbBr_4 and PEA_2PbI_4, respectively. For TOF PET, ℓ of PEA_2PbI_4 is still four times shorter than that of commercial scintillator, LYSO:Ce [8]. For the estimation of theoretical light yield, we calculate the optical bandgap E_g Ref. [1] from the calculated density of states (DOS) using DFT in Fig. 1e. The projected DOS exhibits calculated bandgap E_g^{cal} of 2.13 eV and a defect state at energy of ~0.3 eV below the conduction band minimum similar with that was previously observed [18]. E_g^{cal} is slightly larger than that of 2.06 eV reported in Ref. [31].

After the growth, structure characterization, and material simulation, we perform optical and X-ray scintillation measurements of PEA_2PbI_4 crystal as presented in Fig. 2, PL spectra recorded at RT in Fig. 2a exhibit two different emission origins for two different excitation wavelengths. On the one hand, when we excite the sample at 375 nm, one emission band at 523 nm (green) strongly dominates the band at 660 nm (red). On the other hand, the excitation at 532 nm longer than the wavelength of the first emission band yields only one red emission band. The full width at half maximum (FWHM) for the green emission band is 19 nm while that for the red one is 110 nm. Such PL characteristics were observed for PEA_2PbI_4 crystal grown with PbI_2 precursor and a postsynthetic treatment strategy based on phenethylammonium iodide (PEAI) [18]. The green and the red emission bands correspond to the characteristic of exciton emission from inorganic

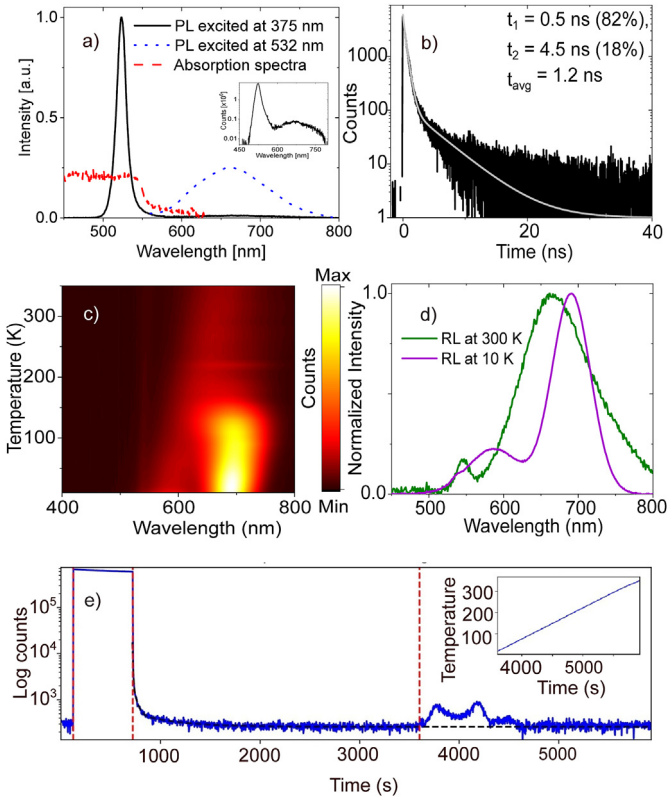

Fig. 2. (a) Absorption and photoluminescence (PL) spectra of single crystal of PEA_2PbI_4 recorded at room temperature (RT). The inset shows the PL spectrum excited at 375 nm with a logarithmic scale of y-axis. (b) Time-resolved PL decay curve excited at 375 nm monitoring 532 nm emission. (c) Radioluminescence (RL) spectra mapping at different temperatures from 10 to 350 K. (d) Representative RL spectra at 10 and 300 K. (e) Steady-state RL, afterglow at 10 K, and temperature-dependent thermoluminescence. Afterglow parts were recorded after 10 min of X-ray irradiation at 10 K with heating rate of 0.14 K/s indicated by the inset.

$[PbI^2]$ layers and surface defect emission, respectively [18]. Absorption spectrum is also shown in Fig. 2a, and the experimental bandgap E_g^{exp} can be estimated to be 2.35 eV (see Fig. S2). E_g^{exp} in our work is slightly smaller than 2.58 eV reported in Ref. [32]. However, if we compare E_g^{exp} with E_g^{cal}, 0.22 eV difference of both values reported in our work is very small comparing to the previous values, and they show the accuracy of our experimental data and simulation for PEA_2PbI_4 crystal. For TRPL in Fig. 2b, we fit the curve with two-exponential decay model. The decay components of 0.5 and 4.5 ns correspond to the exciton emission as the decay curve was recorded by monitoring 532 nm emission wavelength and the average value τ_{avg}^{PL} of 1.1 ns is similar with those reported in Ref. [18]. The average decay time is about six times faster than 6.4 ns day time of PEA_2PbBr_4 crystal [5]. Temperature-dependent RL spectra in Fig. 2c and d show that the emission excited by X-ray is dominated by the red broadband emission of surface defect states, similar to the red emission band in PL spectrum excited at 532 nm in Fig. 2a. The domination of the red surface defect emission against the green exciton emission is due to self-absorption and was frequently observed in BA_2PbBr_4 crystal [5,12]. However, the self-absorption is much stronger in PEA_2PbI_4 crystal as the Stokes shift is only 0.02 eV, much smaller than 0.59 eV in BA_2PbBr_4 crystal [12]. In addition, the peak of this red emission is red shifted from 660 to 690 nm when the temperature decreases from 300 to 10 K. Steady-state RL, afterglow and TL of PEA_2PbI_4 are shown in Fig. 2e. The afterglow part is fitted with three-exponential decay model, and the average decay time for the afterglow is 224 s as shown in Fig. S3. This is 10 times slower than the afterglow of PEA_2PbBr_4 crystal [33], and it is explained by the strong presence of surface defect emission in the RL spectra (Fig. 2d). The TL curve in Fig. 2e shows the presence of the traps, and they look much deeper than those previously in PEA_2PbBr_4 [6,33]. For the analysis of TL through the fit of the glow curve in Fig. S4, the trap depths vary between 0.03 and 0.20 eV while the numbers of traps are in the range of ~10^4. The trap depths are indeed deeper than that of 0.01 eV reported for PEA_2PbBr_4, but the trap numbers are still in the same order [6,33].

Fig. 3a and b presents the results for pulse height spectrum and scintillation decay time curve recorded under γ-ray excitation. Although the pulse height spectrum in Fig. 3a exhibits structures of Compton scattering and photoelectric peak, the energy resolution of 35% is still worse than 7.7% of PEA_2PbBr_4 [33]. We note that the escape peak due to K-shell absorption edge of lead, which is 72 keV at lower energy of the photoelectric peak [5], is not observable in this pulse height spectrum. Therefore, two-peak fitting cannot be performed as in Ref. [33], and the actual energy resolution for PEA_2PbI_4 should be better than 35%. For the light yield derived using single electron response and quantum efficiency of PMT [5], we obtain a value of 1,000 ph/MeV without optical coupling. At 10 K, the light yield increases to 10,000 ph/MeV, see inset of Fig. 3a, and this is still far from fundamental limit of light yield calculated using E_g^{exp} of 170,000 ph/MeV. It is presumably that the light yield quenches at much lower temperature than 10 K and/or loses during self-absorption [5]. However, we found that the light yield is relatively stable if we expose the crystal in the ambient environment for 6 h, see Fig. S5, and this is much better than other iodide scintillators [14]. For the decay curve in Fig. 3b, it shows two additional components in comparison to the PL decay curve in Fig. 2b. The two fast components are similar to those of PL, and they are resolved in the scintillation decay curve with a 50-ns time scale as shown in Fig. S6. The fastest component in scintillation curve is only 0.5 ns and about 10% from

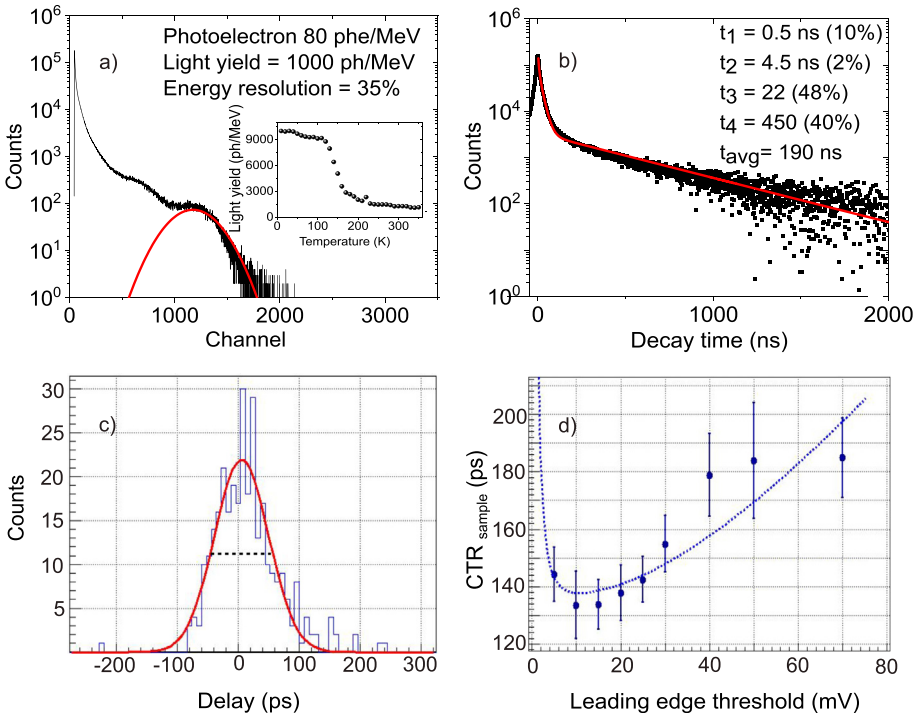

Fig. 3. (a) Integrated pulse height of single crystal of PEA_2PbI_4 in the logarithmic scale. $A^{137}Cs$ source, emitting 662 keV γ-rays, was used as an excitation. The inset shows temperature-dependent light yields derived from pulse height and RL. (b) Scintillation decay curve excited with the same γ-ray source with the red line showing four-exponential-decay fit. (c) Delay distributions at 10 mV with ^{22}Na source emitting two 511 keV γ-rays back-to-back. The red solid lines are the Gaussian functions, which fit the distributions, and the black dotted lines provide the full width at half maximum (FWHM) of the distributions. (d) CTR_{sample} vs. leading edge threshold values. CTR_{FWHM} fit to the data points is shown as blue dashed lines.

the total light yield. However, with the presence of slow component of 450 ns in the scintillation decay curve, the average decay time τ_{avg}^{scint} is calculated to be 190 ns. According to Ref. [18], the observed slow component is associated with the red broadband emission originating from surface defect states, which is dominant in our RL spectra. We hope that by exposing PEA_2PbI_4 crystal with PEAI treatment [18] or by using Lewis bases as alternative defect passivation strategies, the exciton emission might become more dominant again resulting only in fast components. Such fast components of 0.5 and 4.5 ns are much faster in comparison to that of 13.4 ns in PEA_2PbBr_4 crystal. Comparing with BaF_2 scintillator [34,35], the fast component of 0.5 ns is slightly faster than 0.8 ns. The contribution of the fast component to the total light yield of 10% is also similar to 14%, but the light yield of the fast component is only 100 ph/MeV, which is still much smaller than 1,400 ph/MeV of BaF_2 scintillator. (For the detailed comparison of scintillation properties of PEA_2PbI_4 with BaF_2 and some other 2D HOIP scintillators previously reported in the literature [5], see Supplementary Table S2. We also performed RL analysis in Supplementary Fig. S7 to derive the light yield dependences with respect to different PEA_2PbI_4 synthesis methods (see Supplementary Table S3). Finally, the CTR measurement results for PEA_2PbI_4 crystal are shown in Fig. 3c and d. The details of the analysis and the experiments are similar to those reported for PEA_2PbBr_4 crystal [8], except the optical coupling was not applied to the crystal because of its hygroscopicity. Since we used LSO:Ce:Ca scintillator as a reference, the measured CTR (CTR_{meas}) is given by a combination of the CTR of the PEA_2PbBr_4 crystal and that of reference [36]. To evaluate the CTR of two identical samples (CTR_{sample}), the contribution of the reference crystal (CTR_{ref}) need to be subtracted in quadrature from the measured CTR (CTR_{meas}) as shown in the following equation:

$$CTR_{sample} = \sqrt{2 \cdot CTR_{meas}^2 - CTR_{ref}^2}. \quad (1)$$

From Fig. 3c, we obtain CTR_{meas} from the FWHM of the delay distributions of the events with 511 keV energy depositions in both detectors. After subtracting CTR_{ref} of 61 ps via Eq. (1), we obtain CTR_{sample} of 134 ps for PEA_2PbI_4 crystal.

To determine the best CTR_{FWHM} value, a series of CTR measurements were performed, varying the leading edge threshold set on the oscilloscope. Fig. 3d exhibits CTR_{sample} values vs. leading edge threshold values. As there is an effect of limiting the electronic bandwidth and an influence of the electronic noise to CTR_{FWHM} [21,22], the data points were fitted using an empirical model formulated in [37,38]:

$$CTR_{FWHM}(v|p_0, p_1, p_2) = \sqrt{p_0^2 + (p_1 \cdot v)^2 + \left(\frac{p_2}{v}\right)^2}, \quad (2)$$

where v, p_0, p_1, and p_2 are the leading edge threshold, the intrinsic limit of CTR, the photostatistics effect, and the noise contributions, respectively. From the fits in Fig. 3d, the minimum value CTR_{min} of CTR_{FWHM} for PEA_2PbI_4 crystal was determined to be 138 ps. This number is slightly higher than 100 ps of PEA_2PbBr_4 crystal [8]. However, because CTR approximately corresponds to the square root of the ratio from the fast decay component and the light yield, the 0.5 ns decay time in PEA_2PbI_4 crystal, which is faster than 13.4 ns in PEA_2PbBr_4 crystal, seems to compensate for the low light yield of 1,000 photons/MeV at RT in comparison to that of 10,000 photons/MeV in PEA_2PbBr_4 crystal [33]. Further improvements of the light yield and the decay time through Li doping [33] and suppression defect states [18] will be expected to improve the CTR for beating the current 84 ps record in 2D HOIP crystal, Li-doped PEA_2PbBr_4 crystal.

4. Conclusion

In this article, we present the complete characteristics of scintillation properties of PEA_2PbI_4 crystal, which we compare with the up-to-date best 2D HOIP scintillator, PEA_2PbBr_4 crystal. Based on the results of XRD measurements, the DFT calculations of the electronic band structure and DOS were performed. We obtained theoretical E_g^{cal} and experimental E_g^{exp} values of 2.13 and 2.35 eV, respectively, which both has a smaller difference than in previous works for PEA_2PbI_4 crystal. The calculated ℓ of PEA_2PbI_4 at 50 keV is over twice smaller than that of PEA_2PbBr_4, which shows better potential of PEA_2PbI_4 crystal for X-ray imaging applications. PEA_2PbI_4 crystal has an emission wavelength shifted over 100 nm to the green and red comparing to that of PEA_2PbBr_4 crystal. We observed green emission band peaked at 532 nm when the sample was excited with blue light and red emission band peaked at 660 nm when the sample was excited with green light or X-ray. For the γ-ray spectroscopy, the reported light yield of 1,000 photons/MeV at RT from PEA_2PbI_4 crystal is about 10 times smaller than that of PEA_2PbBr_4 crystal, and the estimated energy resolution of 35% is worse than 7.7% reported for PEA_2PbBr_4. However, for the decay time, the fast component of 0.5 ns is much faster than 13.4 ns of PEA_2PbBr_4 crystal. In general, all those scintillation properties can still be improved with Li doping method or suppression of the defect states to decrease the contribution of the slow decay component. As we are aiming for fast-timing applications, one good comparison is BaF_2 crystal, which is often used for TOF, PET, and positron lifetime studies. Thus, with the characteristics reported previously, the PEA_2PbI_4 crystal shows comparable performance. With the emission bands being positioned more at the red part of the spectrum compared with BaF_2, it can significantly increase the detection efficiency for commercial photodiode readout.

Authors' contribution

D.K. contributed to methodology, formal analysis, investigation, and writing, reviewing, and editing the article. M.M., M.E.W., R.C., M.H.M. contributed to formal analysis, investigation, and reviewing and editing the article. M.A.K. contributed to formal analysis and reviewing and editing the article. E.A. and W.D. contributed to resources, formal analysis, and reviewing and editing the article. D.C. contributed to conceptualization, supervision, formal analysis, investigation, reviewing and editing the article, Funding acquisition. M.D.B. contributed to conceptualization, supervision, formal analysis, resources, writing, reviewing, and editing the article, project administration, Funding acquisition.

Declaration of competing interest

The authors declare that they have no known competing financial interests or personal relationships that could have appeared to influence the work reported in this paper.

Data availability

Data will be made available on request.

Acknowledgments

This work has been performed in the framework of the Crystal Clear Collaboration. M.D.B. acknowledges the starting fund from Lukasiewicz Research Network-PORT. D.K. acknowledges funding from National Science Center, Poland under grant MINIATURA no. 2022/06/X/ST5/00369.

Appendix A. Supplementary data

Supplementary data to this article can be found online at https://doi.org/10.1016/j.mtchem.2023.101455.

References

[1] M.D. Birowosuto, D. Cortecchia, W. Drozdowski, K. Brylew, W. Lachmanski, A. Bruno, C. Soci, X-ray scintillation in lead halide perovskite crystals, Sci. Rep. 6 (2016), 37254.
[2] N. Kawano, M. Koshimizu, G. Okada, Y. Fujimoto, N. Kawaguchi, T. Yanagida, K. Asai, Scintillating organic-inorganic layered perovskite-type compounds and the gamma-ray detection capabilities, Sci. Rep. 7 (1) (2017), 14754.
[3] L. Mao, C.C. Stoumpos, M.G. Kanatzidis, Two-dimensional hybrid halide perovskites: principles and promises, J. Am. Chem. Soc. 141 (3) (2019) 1171–1190.
[4] Y. Lekina, Z.X. Shen, Excitonic states and structural stability in two-dimensional hybrid organic-inorganic perovskites, J. Sci.: Adv. Mater. Devices 4 (2) (2019) 189–200.
[5] A. Xie, F. Maddalena, M.E. Witkowski, M. Makowski, B. Mahler, W. Drozdowski, S.V. Springham, P. Coquet, C. Dujardin, M.D. Birowosuto, C. Dang, Library of two-dimensional hybrid lead halide perovskite scintillator crystals, Chem. Mater. 32 (19) (2020) 8530–8539.
[6] A. Xie, C. Hettiarachchi, F. Maddalena, M.E. Witkowski, M. Makowski, W. Drozdowski, Arramel, A.T.S. Wee, S.V. Springham, P.Q. Vuong, H.J. Kim, C. Dujardin, P. Coquet, M.D. Birowosuto, C. Dang, Lithium-doped two-dimensional perovskite scintillator for wide-range radiation detection, Comms. Mater. 1 (2020) 37.
[7] F. Maddalena, A. Xie, Arramel, M.E. Witkowski, M. Makowski, B. Mahler, W. Drozdowski, T. Mariyappan, S.V. Springham, P. Coquet, C. Dujardin, M.D. Birowosuto, C. Dang, Effect of commensurate lithium doping on the scintillation of two-dimensional perovskite crystals, J. Mater. Chem. C 9 (2021) 2504–2512.
[8] R. Cala', I. Frank, F. Pagano, F. Maddalena, C. Dang, M.D. Birowosuto, E. Auffray, Sub-100-picosecond time resolution from undoped and li-doped two-dimensional perovskite scintillators, Appl. Phys. Lett. 120 (24) (2022), 241901.
[9] F. Maddalena, L. Tjahjana, A. Xie, Arramel, S. Zeng, H. Wang, P. Coquet, W. Drozdowski, C. Dujardin, C. Dang, M.D. Birowosuto, Inorganic, organic, and perovskite halides with nanotechnology for high–light yield x- and γ-ray scintillators, Crystals 9 (2) (2019) 88.
[10] P. Krause, E. Rogers, M.D. Birowosuto, Q. Pei, E. Auffray, A.N. Vasil'ev, G. Bizarri, Design rules for time of flight positron emission tomography (tof-pet) heterostructure radiation detectors, Heliyon 8 (6) (2022), e09754.
[11] L.J. Diguna, S. Kaffah, M.H. Mahyuddin, Arramel, F. Maddalena, S.A. Bakar, M. Aminah, D. Onggo, M.E. Witkowski, M. Makowski, W. Drozdowski, M.D. Birowosuto, Scintillation in (c6h5ch2nh3)2snbr4: green-emitting lead-free perovskite halide materials, RSC Adv. 11 (2021) 20635–20640.
[12] L.J. Diguna, L. Jonathan, M.H. Mahyuddin, Arramel, F. Maddalena, I. Mulyani, D. Onggo, A. Bachiri, M.E. Witkowski, M. Makowski, D. Kowal, W. Drozdowski, M.D. Birowosuto, Ba2xbr4 (x = pb, cu, sn): from lead to lead-free halide perovskite scintillators, Mater. Adv. 3 (2022) 5087–5095.
[13] R. Hofstadter, Alkali halide scintillation counters, Phys. Rev. 74 (1948) 100–101.
[14] M.D. Birowosuto, P. Dorenbos, C.W.E. van Eijk, K.W. Krämer, H.U. Güdel, High-light-output scintillator for photodiode readout: lui3:ce3+, J. Appl. Phys. 99 (12) (2006), 123520.
[15] N.J. Cherepy, G. Hull, A.D. Drobshoff, S.A. Payne, E. van Loef, C.M. Wilson, K.S. Shah, U.N. Roy, A. Burger, L.A. Boatner, W.-S. Choong, W.W. Moses, Strontium and barium iodide high light yield scintillators, Appl. Phys. Lett. 92 (8) (2008), 083508.
[16] A. Bessiere, P. Dorenbos, C. van Eijk, K. Krämer, H. Güdel, C. de Mello Donega, A. Meijerink, Luminescence and scintillation properties of the small band gap compound lai3:ce3+, Nucl. Instrum. Methods Phys. Res. 537 (1) (2005) 22–26.
[17] D. Cortecchia, J. Yin, A. Petrozza, C. Soci, White light emission in low-dimensional perovskites, J. Mater. Chem. C 7 (2019) 4956–4969.
[18] J. Yin, R. Naphade, L. Gutiérrez Arzaluz, J.-L. Brédas, O.M. Bakr, O.F. Mohammed, Modulation of broadband emissions in two-dimensional ⟨100⟩-oriented ruddlesden–popper hybrid perovskites, ACS Energy Lett. 5 (7) (2020) 2149–2155.
[19] S. Kahmann, E.K. Tekelenburg, H. Duim, M.E. Kamminga, M.A. Loi, Extrinsic nature of the broad photoluminescence in lead iodide-based ruddlesden–popper perovskites, Nat. Commun. 11 (1) (2020).
[20] J. de Haas, P. Dorenbos, C. van Eijk, Measuring the absolute light yield of scintillators, Nucl. Instrum. Methods Phys. Res. 537 (1) (2005) 97–100.
[21] J.W. Cates, S. Gundacker, E. Auffray, P. Lecoq, C.S. Levin, Improved single photon time resolution for analog SiPMs with front end readout that reduces influence of electronic noise, Phys. Med. Biol. 63 (18) (2018), 185022.
[22] S. Gundacker, R.M. Turtos, E. Auffray, M. Paganoni, P. Lecoq, High-frequency SiPM readout advances measured coincidence time resolution limits in TOF-PET, Phys. Med. Biol. 64 (5) (2019), 055012.
[23] W. Kohn, L.J. Sham, Self-consistent equations including exchange and correlation effects, Phys. Rev. 140 (1965) A1133–A1138.

[24] G. Kresse, J. Furthmüller, Efficiency of ab-initio total energy calculations for metals and semiconductors using a plane-wave basis set, Comput. Mater. Sci. 6 (1) (1996) 15–50.
[25] G. Kresse, J. Furthmüller, Efficient iterative schemes for ab initio total-energy calculations using a plane-wave basis set, Phys. Rev. B 54 (1996) 11169–11186.
[26] P.E. Blöchl, Projector augmented-wave method, Phys. Rev. B 50 (1994) 17953–17979.
[27] G. Kresse, D. Joubert, From ultrasoft pseudopotentials to the projector augmented-wave method, Phys. Rev. B 59 (1999) 1758–1775.
[28] J.P. Perdew, K. Burke, M. Ernzerhof, Generalized gradient approximation made simple, Phys. Rev. Lett. 77 (1996) 3865–3868.
[29] H.J. Monkhorst, J.D. Pack, Special points for brillouin-zone integrations, Phys. Rev. B 13 (1976) 5188–5192.
[30] S. Grimme, J. Antony, S. Ehrlich, H. Krieg, A consistent and accurate ab initio parametrization of density functional dispersion correction (dft-d) for the 94 elements h-pu, J. Chem. Phys. 132 (15) (2010), 154104.
[31] K.-z. Du, Q. Tu, X. Zhang, Q. Han, J. Liu, S. Zauscher, D.B. Mitzi, Two-dimensional lead(ii) halide-based hybrid perovskites templated by acene alkylamines: crystal structures, optical properties, and piezoelectricity, Inorg. Chem. 56 (15) (2017) 9291–9302.
[32] B. Febriansyah, T.M. Koh, Y. Lekina, N.F. Jamaludin, A. Bruno, R. Ganguly, Z.X. Shen, S.G. Mhaisalkar, J. England, Improved photovoltaic efficiency and amplified photocurrent generation in mesoporous n = 1 two-dimensional lead–iodide perovskite solar cells, Chem. Mater. 31 (3) (2019) 890–898.
[33] F. Maddalena, M.E. Witkowski, M. Makowski, A. Bachiri, Arramel, T. Yang, M.H. Mahyuddin, M. Baravaglio, M. Boutchich, W. Drozdowski, C. Dujardin, M.D. Birowosuto, C. Dang, Photodetection and scintillation characterizations of novel lead-bismuth double perovskite halides, J. Mater. Chem. C 10 (2022) 11266–11275.
[34] R.H. Pots, E. Auffray, S. Gundacker, Exploiting cross-luminescence in baf_2 for ultrafast timing applications using deep-ultraviolet sensitive hpk silicon photomultipliers, Front. Physiol. 8 (2020), 592875.
[35] M. Laval, M. Moszyński, R. Allemand, E. Cormoreche, P. Guinet, R. Odru, J. Vacher, Barium fluoride — inorganic scintillator for subnanosecond timing, Nucl. Instrum. Methods Phys. Res. 206 (1) (1983) 169–176.
[36] E. Auffray, B. Frisch, F. Geraci, A. Ghezzi, S. Gundacker, H. Hillemanns, P. Jarron, T. Meyer, M. Paganoni, K. Pauwels, M. Pizzichemi, P. Lecoq, A comprehensive amp; systematic study of coincidence time resolution and light yield using scintillators of different size, wrapping and doping, in: 2011 IEEE Nucl. Sci. Symp. Conf. Rec., 2011, pp. 64–71.
[37] S. Gundacker, E. Auffray, B. Frisch, P. Jarron, A. Knapitsch, T. Meyer, M. Pizzichemi, P. Lecoq, Time of flight positron emission tomography towards 100ps resolution with l(y)SO: an experimental and theoretical analysis, J. Instrum. 8 (7) (2013). P07014–P07014.
[38] S. Gundacker, R.M. Turtos, N. Kratochwil, R.H. Pots, M. Paganoni, P. Lecoq, E. Auffray, Experimental time resolution limits of modern SiPMs and TOF-PET detectors exploring different scintillators and cherenkov emission, Phys. Med. Biol. 65 (2) (2020), 025001.